Journal of
Materials Chemistry C

Accepted Manuscript

ROYAL SOCIETY OF CHEMISTRY

rsc.li/materials-c

View Article Online
DOI: 10.1039/C7TC05238C

Table of Content Figure

A new kind of a straightforward synthesized and dopant-free hole transporting material designed based on cost efficient anthanthrone dye was implemented successfully in mesoporous perovskite solar cells. This Donor-Acceptor-Donor HTM based device achieves an overall efficiency of 11.5% under 1 sun condition and retains impressive performance during 58% relative humidity than traditional costly SPIRO-OMeTAD.

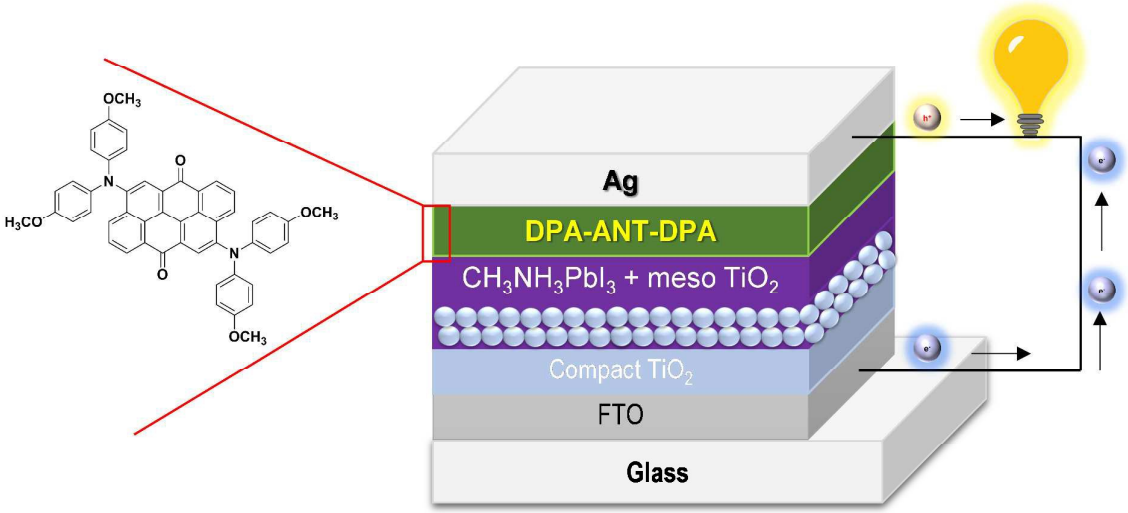

View Article Online
DOI: 10.1039/C7TC05238C

One Step Facile Synthesis of Novel Anthanthrone Dye Based, Dopant-Free Hole Transporting Material for Efficient and Stable Perovskite Solar Cells

Hong Duc Pham,[a]† Kazuma Hayasake,[b] Jinhyun Kim,[c] Thu Trang Do,[a] Hiroyuki Matsui,[b] Sergei Manzhos,[d] Krishna Feron,[e,f] Shizuo Tokito,[b] Trystan Watson,[g] Wing Chung Tsoi,[g] Nunzio Motta,[a] James R. Durrant, [c,g] Sagar Motilal Jain,[g*]† Prashant Sonar[a*]

a. Institute of Future Environment and School of Chemistry, Physics and Mechanical Engineering, Queensland University of Technology (QUT), 2 George Street, Brisbane, QLD-4001, Australia.

b. Research Center for Organic Electronics (ROEL), Yamagata University, 4-3-16 Jonan, Yonezawa, Yamagata 992-8510, Japan.

c. Department of Chemistry and Centre for Plastic Electronics, Imperial College London, Exhibition Road, London SW7 2AZ, United Kingdom.

d. Department of Mechanical Engineering, Faculty of Engineering, National University of Singapore.

e. CSIRO Energy Centre, NSW-2304, Australia.

f. Centre for Organic Electronics, University of Newcastle, Callaghan, NSW 2308, Australia.

g. SPECIFIC, College of Engineering, Swansea University Bay Campus, Fabian Way, SA1 8EN Swansea, United Kingdom.

† These authors, H. D. P and S. M. J contributed equally to the work.

Electronic Supplementary Information (ESI) available: [details of any supplementary information available should be included here]. See DOI: 10.1039/x0xx00000x

View Article Online
DOI: 10.1039/C7TC05238C

Abstract:

Perovskite solar cell (PSCs) technology has made a tremendous impact in the solar cell community due to their exceptional performance, as the power conversion efficiency (PCE) surged to world record 22% within just last few years. Despite this high efficiency value, the commercialization of PSCs for large area applications at affordable prices is still pending due to the low stability of devices in ambient atmospheric conditions and a very high cost of the hole transporting materials (HTM) used as the charge transporting layer in such devices. To cope with these challenges, the use of cheap HTMs can play a dual role in terms of lowering the overall cost of the perovskite technology as well as protecting the perovskite layer to achieve higher stability. In order to achieve these goals, various new organic hole transporting materials (HTMs) have been proposed. In this work we use a unique and novel anthanthrone (ANT) dye as a conjugated core building block and an affordable moiety to synthesize a new HTM. The commercially available dye was functionalized with an extended diphenylamine (DPA) end capping group. The newly developed HTM, named DPA-ANT-DPA, was one-step synthesized and used successfully in mesoporous perovskite solar cell devices, achieving a PCE of 11.5% under 1 sun condition with impressive stability. The obtained device efficiency is amongst the highest, as per D-A-D molecular design and low band gap concern. Such kind of low cost HTM based on inexpensive starting precursor anthanthrone dye paves the way for economical and large-scale production of stable perovskite solar cells.

View Article Online
DOI: 10.1039/C7TC05238C

Introduction

The number of potentially economic solar cell technologies is increasing every year, in search of the Holy Grail of maximum conversion efficiency and minimum production cost. In the area of low cost solar cells, which includes as organic solar cells and dye sensitized solar cells (DSSC), organic–inorganic halide perovskite solar cells (PSCs) have gained much attention from the scientific community as scientists have been able to quickly achieve record performances, unparalleled in organic and DSSC. After the first breakthrough in 2013, the power conversion energy (PCE) for PSCs achieved a value of 22.1%,[1, 2] very close to that of traditional silicon solar cells. Nevertheless, a few major obstacles are yet to be addressed before the commercial application of this technology. The first challenge is to improve the stability of the solar cells. The second one is how to enhance the performance in terms of PCE. The hole transporting layer (HTL) plays an extremely important role in both stability and performance of the perovskite solar cells. It improves the device stability by preventing the contact of the active perovskite layer with the metal electrode, blocking moisture and oxygen penetration.[3] HTL is also instrumental in suppressing charge recombination allowing to achieve a higher open-circuit photovoltage (V_{oc}), which leads to greater efficiency.[4-6] One of the key components responsible for the high cost of perovskite solar cells, is the hole transporting materials (HTL): in fact the most efficient and widely used HTL is the molecule: 2, 2', 7, 7'-tetrakis-(*N*,*N*-di-*p*-methoxyphenylamine)-9,9'-spiro-bifluorene (Spiro-OMeTAD). Unfortunately, the very high cost of the Spiro-OMeTAD molecule (400 USD per gram) limit the large scale production of perovskite solar cells. In order to make this technology more economical viable, there is a great need to find alternative HTLs with lower cost, simple synthesis, which would also be easily scalable and which can achieve equal or higher performance than the Spiro-OMeTAD. Currently, several economical organic hole transporting materials (HTMs) employed in PSCs show respectable efficiency and higher stability compared to Spiro-OMeTAD. Among them, small molecular HTMs are advantageous compared to polymeric counterparts because of their high purity, defined molecular structure, promising yield, and better batch-to-batch reproducibility.[7-9]

In the group of small molecules, abundant rational molecular design strategies, including donor-π-donor (D-π-D), acceptor-donor-acceptor (A-D-A) and donor-π-acceptor (D-π-A) moieties, have been intensively used for synthesis. Perovskite

View Article Online
DOI: 10.1039/C7TC05238C

devices with higher performance and better stability have been fabricated successfully using such HTMs. For example, (*E*)-4′,4‴-(ethene-1,2-diyl)bis(*N*,*N*-bis(4-methoxyphenyl)-[1",1"'-biphenyl]-4-amine) (TPA-BPV-TPA) (16.42%),[10] 2′,7′-bis(bis(4-methoxyphenyl)amino)spiro[cyclopenta[2,1-b:3,4-b′]dithiophene-4,90-fluorene] (FDT) (20.2%),[11] *N*-(4-(9*H*-carbazol-9-yl)phenyl)-7-(4-(bis(4-methoxyphenyl)amino)phenyl)-*N*-(7-(4-(bis(4-methoxyphenyl)amino)phenyl)-9,9-dioctyl-9*H*-fluoren-2-yl)-9,9-dioctyl-9*H*-fluoren-2-amine (CzPAF-TPA) (15.71%),[12] 4,4′-(5,5′-(7,7′-(5,5′-(4,8-bis((2-ethylhexyl)oxy)benzo[1,2-b:4,5-b′]dithiophene-2,6-diyl)bis(3-hexylthiophene-5,2-diyl))bis(benzo[c][1,2,5]thiadiazole-7,4-diyl))bis(4-hexyl-thiophene-5,2-diyl))bis(1-(2-ethylhexyl)pyridin-1-ium) bis(trifluoromethane sulfonimide) (M7-TFSI) (17.4%),[13] and 2,2′,2″-(((5,10,15-trihexyl-10,15-dihydro-5H-diindolo[3,2-a:3′,2′-c]carbazole-3,8,13-triyl)tris(3,3″-dihexyl-[2,2′:5′,2″-terthiophene]-5″,5-diyl))tris(methanylylidene))trimalononitrile (KR321) (19.03%).[14] These HTMs can lead an efficiency in the range of 16-20%. However, there are few new HTMs based on D-A-D structure reported until now, including 4,4′-(1,3,4-Oxadiazole-2,5-diyl)bis(*N*,*N*-bis(4-methoxyphenyl)aniline) (H1),[15] 4,4′-(5,6-dimethoxybenzo[c][1,2,5]oxadiazole-4,7-diyl)bis(*N*,*N*-bis(4-methoxyphenyl)aniline) (BTPA-3),[6] (9,9'-((benzo[c][1,2,5]thiadiazole-4,7-diyl)bis(4,1-phenylene))bis(N^3,N^3,N^6,N^6-tetrakis(4-methoxyphenyl)-9*H*-carbazole-3,6-diamine) (JY5)[16] and (9,9'-((5-fluorobenzo[c][1,2,5]thiadiazole-4,7-diyl)bis(4,1-phenylene))bis(N^3,N^3,N^6,N^6-tetrakis(4-methoxyphenyl)-9*H*-carbazole-3,6-diamine) (JY6).[17] The D-A-D structure has been designed by introducing an electron-deficient unit as the core with two strong electron-rich end-capping groups in order to obtain a deeper highest-occupied molecular orbital (HOMO) level, thereby improving the V_{oc}.[18] This strategy is expected to result in a higher PCE.[5, 10, 19-21] In addition, compared to the D−π–D type molecules, the intramolecular charge transfer (ICT) from the electron-donating unit to the electron-withdrawing unit can be boosted via the D-A-D one.[6]

In this work, we report one-step facile synthesis of a novel dopant-free D-A-D HTM based on a low cost anthanthrone (ANT) dye as the core and diphenylamine (DPA) as an efficient end-capping conjugated building block. The compound, namely 4,10-bis(bis(4-methoxyphenyl)amino)naphtho[7,8,1,2,3-*nopqr*]tetraphene-6,12-dione (DPA-ANT-DPA) is synthesized using standard Buchwald coupling between the halogenated derivative and the amine group; the synthesis details are shown in Scheme

View Article Online
DOI: 10.1039/C7TC05238C

1. In this D-A-D type structure, 4,10-dibromoanthanthrone, named as VAT Orange 3 (Compound 1 in Scheme 1) low cost starting precursor was introduced as a strong electron-withdrawing ketone unit in the core due to its π–conjugated nature and a large conjugated planar structure.[22-24] This is profitable for obtaining a low-lying HOMO energy level,[25] improving intermolecular interactions such as π–π interactions[22] and achieving the high performance of organic optoelectronic devices.[25]

Results and Discussion

The synthesis of DPA-ANT-DPA is straightforward and follows Buchwald-Hartwig coupling reaction. Compound 1 and 2 were mixed with [1,1′-Bis(diphenylphosphino)ferrocene] dichloropalladium(II) [$PdCl_2$(dppf)] catalyst at 90 °C for 24 h in anhydrous toluene solvent as the earlier attempt.[26] After purification by column chromatography, the yield of the reaction was found to be of 80%, leading to potential large-scale application in the future. The purity was confirmed by proton and carbon NMR spectroscopy, the results of which are shown in Fig. S1 (Supporting Information, ESI†). The synthetic procedure is detailed in the ESI†. The material exhibited good solubility in most common organic solvents such as chloroform, dichloromethane and chlorobenzene.

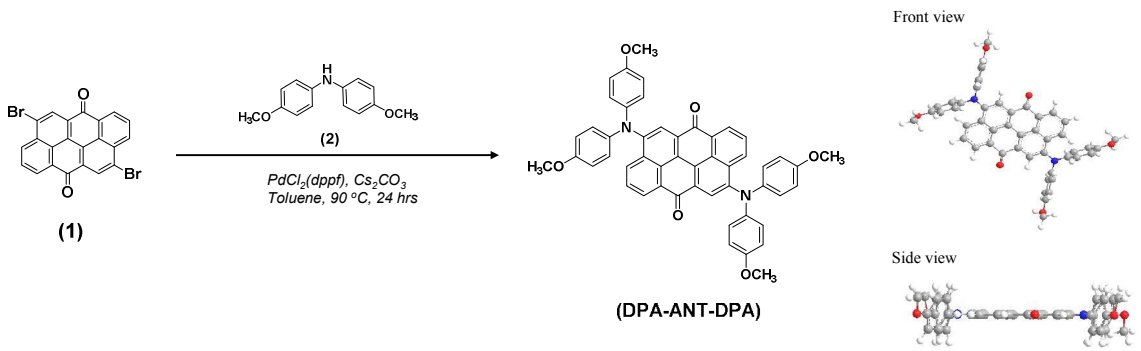

Scheme 1. A single-step synthetic route for DPA-ANT-DPA and the geometrical configuration (front and side view).

To gain insight into the electronic structure of this material, density functional theory (DFT) calculations were performed at the B3LYP level of theory using the basis set 6-31g+(d,p).[27-29] As shown in Fig. 1a, while the electron density of the HOMO is fully delocalized over the entire molecules, the lowest unoccupied molecular orbital (LUMO) is primarily distributed over the π-conjugated system through the ANT core. According to DFT calculations, the HOMO and LUMO value are assessed to be -4.79 eV and -3.01 eV respectively. As a result, the band gap is found to be of 1.78 eV. In addition, the optical

View Article Online
DOI: 10.1039/C7TC05238C

absorption maxima were at 892 nm, resulting to the optical band gap of 1.39 eV. The DFT-calculated data differs slightly from the experimental values due to the gaseous state assumptions, but the result is still in a good agreement (Table 1).

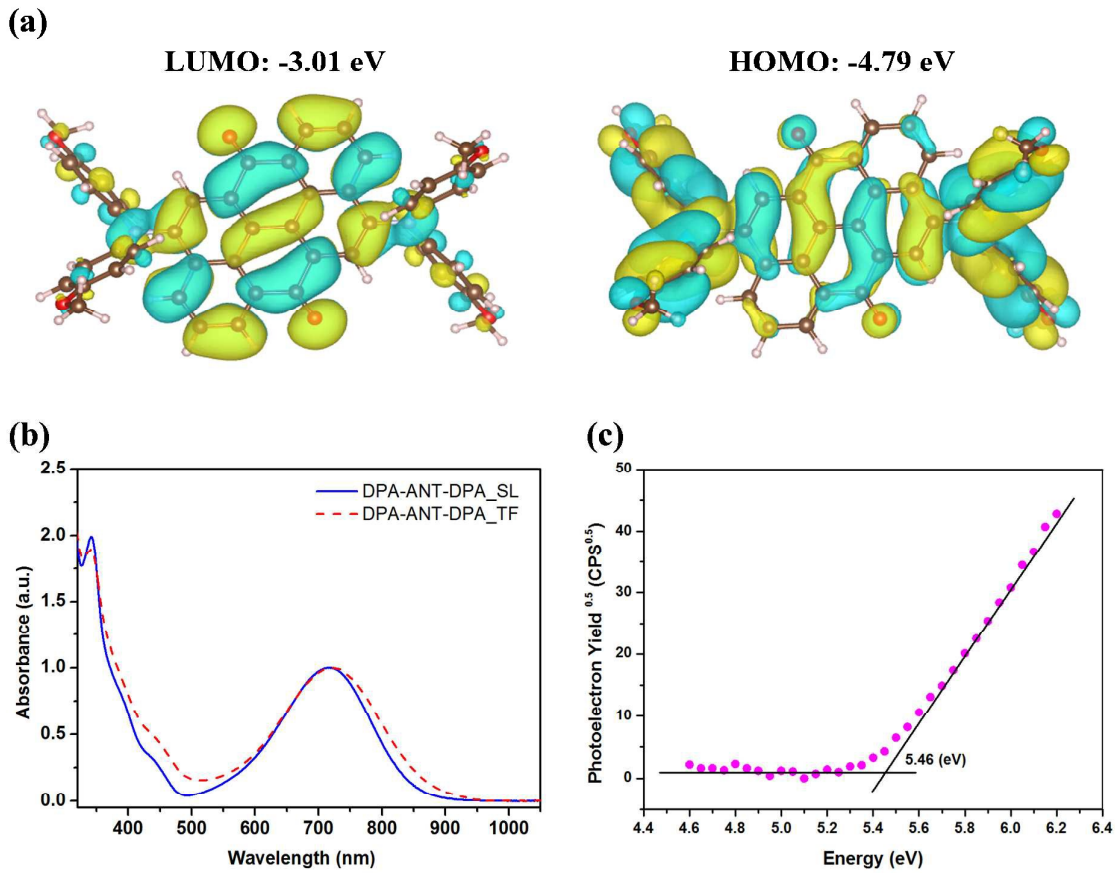

Fig. 1 (a) The calculated isosurfaces of electron density of HOMO and LUMO, (b) UV-Vis absorption spectra in CF solutions (solid line) and films (dash line), (c) Photoelectron spectroscopy in air (PESA) spectra of DPA-ANT-DPA.

The absorption of DPA-ANT-DPA in chloroform solution and in thin film on glass were measured and shown in Fig. 1b. All the data is listed in Table 1. In the low wavelength region, DPA-ANT-DPA reveals absorption maxima at 344 nm for the solution and 343 nm for thin film respectively. Meanwhile, it shows broaden absorption in the visible range with maxima peak at 717 nm in solution and 724 nm in solid-state film respectively. The electronic absorption in the near-infrared (NIR) region is attributed with the ICT band due to the introduction of strong electron donating DPA end capping units and strong electron accepting ANT core.[30, 31] The slight red shift of the absorption band in films compared with solution indicates very weak intermolecular interactions in the solid state. Such weak solid-

View Article Online
DOI: 10.1039/C7TC05238C

state interaction is also arising due to the presence of two distorted phenylene units. Such propeller structure could be beneficial to form a better interface with three dimensional photoactive perovskite layers in the devices, which can promote charge transport effectively. The optical band gap of DPA-ANT-DPA compound, calculated using the solid-state absorption onset values at 869 nm, is 1.43 eV. This low band gap implies a strong intramolecular D-A interaction in relative to the amine and quinone units as mentioned previously.[26] To the best of authors knowledge, it is the lowest band gap HTM for PSCs compared to other low band gap HTMs (1.47 – 1.50 eV) reported previously.[30, 32, 33]

Table 1 Thermal, optical and electrochemical properties of DPA-ANT-DPA.

HTMs	λ_{max} (nm)		λ_{onset} (nm)	E_g^{opt} [c)] (eV)	E_{HOMO} [d)] (eV)	E_{LUMO} [d)] (eV)	E_{HOMO} [e)] (eV)	T_d (°C)	T_g (°C)	T_c (°C)	T_m (°C)	μ [f)] ($cm^2V^{-1}s^{-1}$)
	Solution[a)]	Film[b)]										
DPA-ANT-DPA	292	294	869	1.43	-5.46	-4.03	-5.2	377	148	244	294	1×10^{-4}

[a)]Absorption spectrum was measured in chloroform (CF) solution; [b)]Film was prepared by spin-coating an CF solution containing the sample onto glass substrate at a spin speed of 1000 rpm at room temperature; [c)]Optical bandgap was calculated from the formula of $1240/\lambda_{onset}$; [d)]The oxidation potential was also measured by photoelectron spectroscopy in air (PESA); $E_{LUMO}^{PESA}=E_{HOMO}^{PESA}+E_g^{opt}$; [e)]Oxidation potential of the material was characterized in dichloromethane with 0.1 M tetrabutylammonium hexafluorophosphate at scan speed 100 mV/s, potentials vs. Fc/Fc^+; [f)]hole mobility was measured by space charge limited current (SCLC) method.

In this work we determine the HOMO value of DPA-ANT-DPA experimentally using two methods such as photoelectron spectroscopy in air (PESA) (Fig. 1c) and cyclic voltammetry (CV) respectively (Fig. S2, ESI†). All these parameters are shown in Table 1. The HOMO value of DPA-ANT-DPA is estimated to be -5.46 eV, being similar to the valence band maximum (VBM) of the perovskite layer. The reduced energy gap between the HTL and the active layer guarantees a high valued for of V_{oc} and also keeps efficient hole extraction. Meanwhile, the respective LUMO level of this compound was estimated, based on $E_{LUMO} = E_{HOMO} + \boldsymbol{E_g^{opt}}$, to be found of -4.03 eV. This low-lying LUMO energy level is below the conduction band minimum (CBM) of the perovskite, which allows part of undesired electron transport to occur and then cause to the low efficiency. While the LUMO value obtained by CV data is in consistent with the calculation one from PESA data, the HOMO values from both techniques are slightly different. This may be caused by the energy values of sample in CV technique which was performed in dichloromethane solution with tetrabutylammonium

View Article Online
DOI: 10.1039/C7TC05238C

hexafluorophosphate. Whereas, in PESA, the sample is deposited in thin film and then exposed to ultraviolet light with certain intensity in air. The HOMO energy value data from the PESA technique is more relevant since the actual devices in solid state and the PESA measurement also performed in thin film form.

The thermal properties of DPA-ANT-DPA were determined by using thermogravimetric analysis (TGA) and differential scanning calorimetry (DSC), which are shown in Fig. S3 (ESI†) and summarized in Table 1. According to the TGA curve, this compound has an extremely good thermal stability, and is stable up to 377 ^{o}C. The thermal transitions were investigated by DSC with two scan cycles. The melting temperature (T_m) (294 ^{o}C) is observed during the first and second heating scans whereas the glass transition (T_g) (148 ^{o}C) is only noticed during the second heating scan. Furthermore, the crystallization temperature (T_c) is witnessed at 244 ^{o}C during the second heating scan. It turns out that the material has some crystalline phases and this might be arising from donor-acceptor interaction and fused core nature of ANT conjugated building block.[34] This is in good agreement with the observation of the needle-like crystals' formation during drying process of DPA-ANT-DPA solution in the glass tube (Fig. S4, ESI†). Meanwhile, there is no crystallization peaks perceived during the cooling step. Furthermore, X-ray diffraction (XRD) was performed with the result shown in Fig. S5 (ESI†). The primary intense peak at $2\theta = 9.34^{o}$ was observed, leading to a d-spacing (the lamellar repeating distance between the compound chains) of 1.1 nm calculated by using Bragg equation.

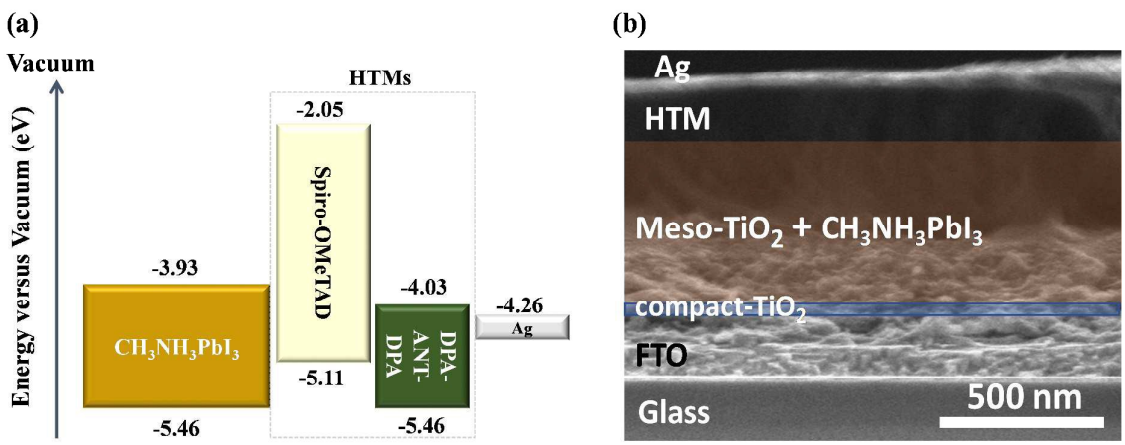

Fig. 2 (a) Energy level diagrams, (b) Cross-sectional scanning electron microscopy image of PSC of DPA-ANT-DPA.

View Article Online
DOI: 10.1039/C7TC05238C

In order to evaluate the effect of such crystalline phases on the charge carrier transport, we used DPA-ANT-DPA material as an active layer in organic field-effect transistor (OFET) devices using bottom gate top contact devices. The OFET device fabrication is described in ESI†. Its data is shown in Table 1 and illustrated in Fig. S6 (ESI†). The hole mobility of DPA-ANT-DPA was calculated using output and transfer characteristics. The mobility of DPA-ANT-DPA was calculated to be 2.6×10^{-4} $cm^2V^{-1}s^{-1}$, which is higher than that of Spiro-OMeTAD ($\mu = 1.69\times10^{-6} - 2.3\times10^{-5}$ $cm^2V^{-1}s^{-1}$)[35, 36] measured with a similar experimental technique (using OFET devices). Furthermore, we measured and compared the hole mobility of our newly developed DPA-ANT-DPA and of the traditional Spiro-OMeTAD hole transport layers (Fig. S7, ESI†) using hole only space charge limited current method using identical conditions. The hole mobility for DPA-ANT-DPA is 1 x 10^{-4} $cm^2V^{-1}s^{-1}$ whereas for Spiro-OMeTAD it is 1.6 x 10^{-4} respectively measured by SCLC method. As per solar cell devices concern, SCLC measurement is most relevant techniques which give correct charge carrier mobility since the charge transport occurs vertically. The details of sample preparation and SCLC measurement can be found in supporting information (ESI†). Bopth OFET and SCLC techniques confirms the better charge carrier mobility of our newly developed hole transport layers DPA-ANT-DPA .

After the optical, thermal and electrochemical characterization of the new small molecule, the DPA-ANT-DPA layer was fabricated within the conventional perovskite devices processing as HTM, with the main aim to study the effect of the hole transport layers on the device performance. PSC devices with the FTO/compact-TiO_2/Mesoporous-TiO_2/$CH_3NH_3PbI_3$/HTL/Ag device architecture were fabricated as per previously reported procedure.[37] The configuration of mesoscopic heterojunction perovskite solar cells was characterized by the cross-sectional scanning electron microscopy (SEM) and shown in Fig. 2b. A dense compact-TiO_2 blocking layer (~30 to 40 nm) is first deposited on the FTO substrate by spray pyrolysis, while a mesoporous n-type mp-TiO_2 layer is formed by spin-coating of diluted TiO_2 paste. The $CH_3NH_3PbI_3$ absorber layer was then applied on mesoporous TiO_2 by solvent engineering reported by Seok's group.[37]

The perovskite solution was prepared as per standard procedure and details can be found in the supporting information (ESI†). Around 120 nm thick HTLs were applied to the top $CH_3NH_3PbI_3$ layer by spin coating. Finally, silver as a counter electrode was deposited by thermal evaporation. The thickness of mesoporous TiO_2 and perovskite is ~550 nm, whereas

View Article Online
DOI: 10.1039/C7TC05238C

the capping layer of perovskite is estimated to be ~100 nm. Bigger crystals of TiO_2 in the capping layer assist in saturated light absorption, which enhances the external quantum efficiency (EQE) in the red-light range.

For a valid comparison of performance in terms of PCE and stability, we prepared new dopant-free HTMs based devices and standard devices with dopant using conventional Spiro-OMeTAD (with additional additives, including *t*BP and LiTFSI) as the HTM. The optimized champion device efficiency for DPA-ANT-DPA and Spiro-OMeTAD HTMs and corresponding photovoltaic performance parameters are shown in Fig. 3 and Table 2.

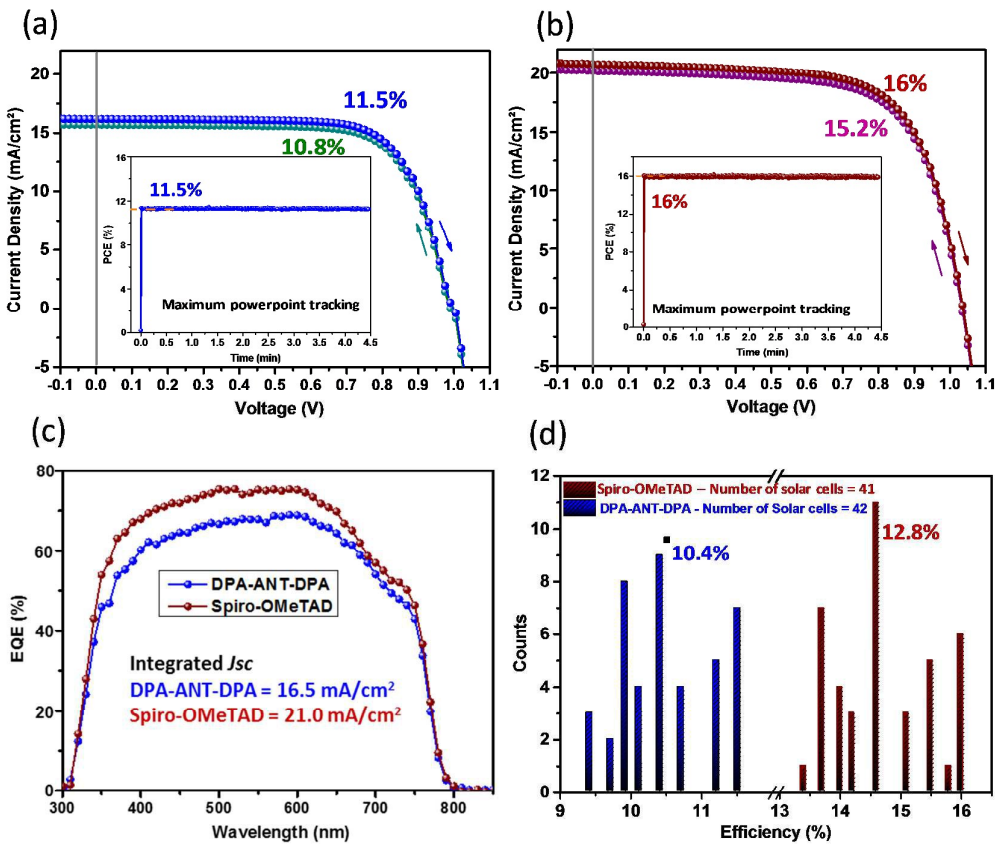

Fig. 3 Current–voltage scans for the best performing perovskite devices made using (a) DPA-ANT-DPA as hole transport layer and (b) Spiro-OMeTAD as hole transport layer showing PCEs 11.3% and 14.3% respectively. The full hysteresis loop is reported in Table 2. The inset shows the power output under maximum power point tracking for 270 s, starting from forward bias and resulting in a stabilized power output of 11.5% and 16% for DPA-ANT-DPA and Spiro-OMeTAD hole transport based devices respectively. The constant scan rate for all scans was 10 mV s−1, (c) External quantum efficiency of perovskite devices prepared using DPA-ANT-DPA and Spiro-OMeTAD hole transport materials. The integrated short

View Article Online
DOI: 10.1039/C7TC05238C

circuit current density of 16.5 mA/cm^2 and 21 mA/cm^2 follows the JV scans from the solar simulator, (d) Statistics, and the average device efficiency of a total of 83 solar cells prepared using DPA-ANT-DPA and Spiro-OMeTAD as hole transport materials.

The non-doped DPA-ANT-DPA HTM based PSC devices (Fig. 3a) shows the highest champion device efficiency of 11.5% (J_{sc} = 16.2 mA cm^{-2}, V_{oc} = 1.0 V and *FF* = 71%). Whereas the doped Spiro-OMeTAD-based device performance (Fig. 3b) approaches a PCE of 16 % with J_{sc} of 21 mA cm^{-2}, V_{oc} = 1.03 V and *FF* = 74%. The hysteresis behaviour of champion devices and statistics of the total of 42 devices prepared using DPA-ANT-DPA and 41 devices using Spiro-OMeTAD as hole transporting layers is shown in Table 2 and Fig. 3(a),(b) respectively.

Table 2 Solar cell device performance with DPA-ANT-DPA HTMs.

HTLs	Scan Direction	V_{oc} (V)	J_{sc} (mA/cm^2)	FF (%)	PCE (%)
DPA-ANT-DPA[b)]	Forward	1.00	16.2	71	11.5
	Reverse	0.98	15.8	69	10.8
	Average[d)]	0.97	15.0	69	10.4
Spiro-OMeTAD[c)]	Forward	1.03	21.0	74	16.0
	Reverse	1.03	20.4	72	15.2
	Average[d)]	0.99	18.2	71	12.8

[a)] Cell size (active area): 0.100 cm^2. Photovoltaic performance at 1000 wm^{-2} (AM1.5G) and constant scan speed of 10 mV s^{-1} mesoscopic $CH_3NH_3PbI_3$ devices; [b)]without additives; [c)]with additives: 4-tert-butylpyridine (*t*BP) and Li-bis(trifluoromethanesulfonyl)-imide (LiTFSI); [d)]An average device efficiency of a total of 41 and 42 devices for Spiro-OMeTAD and DPA-ANT-DPA, respectively.

View Article Online
DOI: 10.1039/C7TC05238C

We observed a negligible hysteresis on the reverse scan (0 V to V_{oc}) at a low scan speed of 10 mV s^{-1} for DPA-ANT-DPA and Spiro-OMeTAD based devices that results in the efficiency decrease from 16% to 15.2% for Spiro-OMeTAD based and 11.5% to 10.8% for DPA-ANT-DPA HTM based perovskite solar cells. The excessively small band offset of the HOMO between perovskite and DPA-ANT-DPA HTL (as shown in Fig. 2(a)), may hamper the effective hole transport ability.[38] We observed that even though the work function of DPA-ANT-DPA is very close to that of the perovskite active layer, a respectable PCE could still be achieved, without doping. The good comparable V_{oc} of 1.0 V for DPA-ANT-DPA to that of Spiro-OMeTAD based devices is due to the very small band offset and HOMO value difference between this compound and perovskite active layer.[38] Furthermore, the non-doped DPA-ANT-TPA based PSC shows a short circuit current (J_{sc} = 16.2 mA cm^{-2}) comparable to that with Spiro-OMeTAD (J_{sc} =21 mA cm^{-2}) which is due to the shallower HOMO of DPA-ANT-DPA that allows for effective hole extraction.

The PCE of 11.5%, obtained using non-doped DPA-ANT-DPA HTM, is high compared to other HTMs reported in the literature taking dopant-free aspect into account.[4, 39-41] As shown in Fig. 3c, the devices with DPA-ANT-DPA exhibit external quantum efficiency (EQE) values above 65 to 70% from 365 nm to 650 nm covering the entire UV region with the highest EQE of 70% observed at 470 nm. The statistics of total 83 PSCs prepared using DPA-ANT-DPA and Spiro-OMeTAD as shown in Fig. 3d exhibits an average device efficiency of 10.4% and 12.8% respectively.

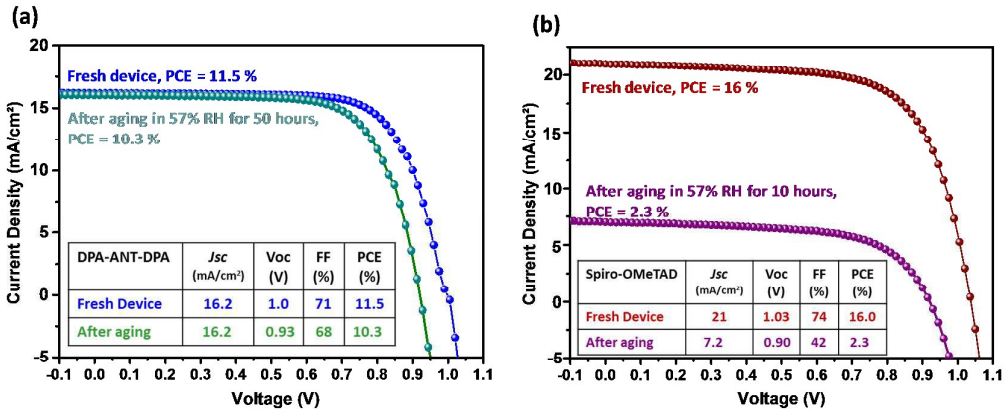

Fig. 4 Photovoltaic performance of DPA-ANT-DPA (a), and Spiro-OMeTAD (b) based $CH_3NH_3PbI_3$ PSC devices respectively on aging in humidity ≥ 57% (the fresh and aged PSC devices performance is shown in satellite table); Stability test/aging for 50 hours for DPA-ANT-DPA HTM based cells and 10 hours for Spiro-OMeTAD HTM based PSC: without

View Article Online
DOI: 10.1039/C7TC05238C

encapsulation. After each consecutive measurement, the PSCs are kept in an ambient humidity setup of RH of 57%, Temperature = 22 ^{o}C.

The stability of PSCs is one of the most discussed issues within the perovskite solar cell community and a major hurdle for commercialization. Since the active layer in perovskite devices is an organometallic salt, it has a strong tendency to absorb water. Among different degradation factors, ambient humidity is one of the most critical parameters being for the degradation of Spiro-OMeTAD based PSCs and this is due to the hydrophilic nature of the active layer used in PSC.[42-44] Taking these parameters into account, we studied the stability of fabricated champion devices without any encapsulation at high humidity conditions (relative humidity (RH) = 57%, temperature = 22 ^{o}C, in dark condition) for our newly developed DPA-ANT-DPA and standard Spiro-OMeTAD HTMs (as shown in Fig. 4).

A simple stability setup used is shown in Fig. S8 a,b (ESI†) and the photovoltaic performance was measured at 1000 wm^{-2} (AM1.5G) using regular aging intervals. The photovoltaic properties of our novel DPA-ANT-DPA and Spiro-OMeTAD in the aging test are detailed in Fig. 4a and 4b. Additionally, the efficiency of all HTMs based devices is evaluated under identical conditions and depicted in Fig. 4. The degradation test results show that the Spiro-OMeTAD HTM based devices degraded at a faster rate compared to DPA-ANT-DPA based devices. The Spiro-OMeTAD HTM based devices showed a rapid drop in PCE from 14.2% (Fresh device) to 2.3% after aging in 57% RH, for only 10 hours. Spiro-OMeTAD HTM based devices showed significant drop in current from J_{sc} = 21 to 7.1 mA/cm^2. On the other hand, the DPA-ANT-DPA HTM based devices maintained the *Jsc* of 16 mA/cm^2 with a very small drop in open circuit voltage V_{oc} from 1.0 to 0.93 V. This resulted in a small drop in PCE from 11.5% to 10.3%, this is even after prolonged exposure of 50 hours to high relative humidity of 57%. This clearly shows improved device stability of PSCs made using DPA-ANT-DPA HTM over Spiro-OMeTAD based devices.

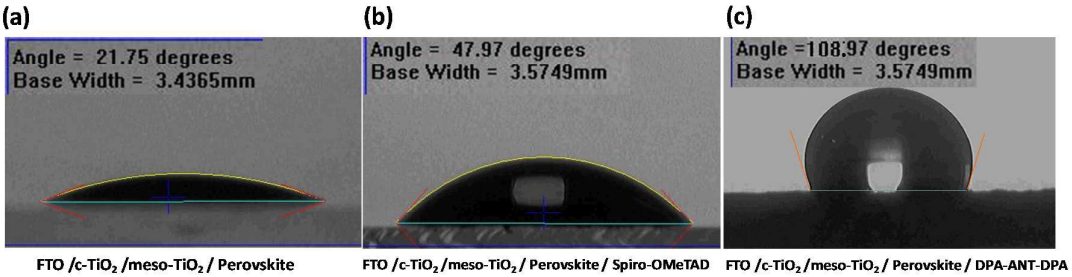

View Article Online
DOI: 10.1039/C7TC05238C

Fig. 5 Contact angle measurements performed on (a) $CH_3NH_3PbI_3$ perovskite, (b) Spiro-OMeTAD and (c) DPA-ANT-DPA surface, deposited on FTO/c-TiO_2/meso-TiO_2 substrate.

To further investigate the reason for the dramatic improvement in stability of DPA-ANT-DPA (compare to Spiro-OMeTAD) based PSCs. Considering that the top layer of the perovskite solar cell device plays an important role in preventing water ingress,[45] we performed contact angle measurements (as shown in Fig. 5(a-c)) as well morphological measurements on the top surface of PSCs, which is the surface of HTMs (as shown in Fig. 6).

Fig. 5 (a) shows a low contact angle of 21^o of a water droplet on $CH_3NH_3PbI_3$ surface, this confirms the good wetting behaviour, high hydrophilic nature of the $CH_3NH_3PbI_3$ perovskite active layer used in this study. Doped Spiro-OMeTAD layers, deposited on top of the perovskite shows a contact angle of 47.9^o, indicating a reduced albeit still high degree of hydrophilicity of the overall device. Snaith et al already demonstrated the cause behind hydrophilic nature of Spiro-OMeTAD based HTM devices and this is mainly due to the doping of Spiro-OMeTAD using hygroscopic LiTFSI salts.[45] We would like to make clear that though the Spiro-OMeTAD molecule itself is non-polar by nature due to the presence of four methoxy groups on phenylene units, it becomes hydrophilic owing to the addition of dopant salts. The contact angle measured using our newly developed DPA-ANT-DPA HTMs surface without using any dopant leads to an impressive elevated contact angle of 108^o with lower wetting (enhancing hydrophobicity); this is likely mainly responsible for higher stability of reported devices here using our new HTM.

Moreover, it is further necessary to study the surface morphology of the HTMs in order to understand the different wetting, de-wetting behaviour and hence to probe the reason for the hygroscopic nature of the films. Fig. 6 shows surface morphology of the perovskite, DPA-ANT-DPA and Spiro-OMeTAD hole transport layer. The $CH_3NH_3PbI_3$ perovskite film Fig. 6 (a) shows good quality, larger crystalline grains ranging from 500 - 800 nm. The good quality of the perovskite film is further confirmed from high photoluminescence (PL) intensity obtained (Fig. 7). The HTM DPA-ANT-DPA deposited on perovskite shows homogeneous, uniform surface coverage over a large area (Fig. 6(b)), while the Spiro-OMeTAD deposited on perovskite shows inhomogeneous and rough surface also formation of small aggregates at intervals, as shown in Fig. 6(b-c). These are possibly the crystals formed due to doping of LiTFSI.[46] This is further confirmed from the observation that in absence of doping with

View Article Online
DOI: 10.1039/C7TC05238C

tertiary butyl pyridine (*tBP*) and LiTFSI salts in Spiro-OMeTAD, we have not observed such aggregate formation**.**

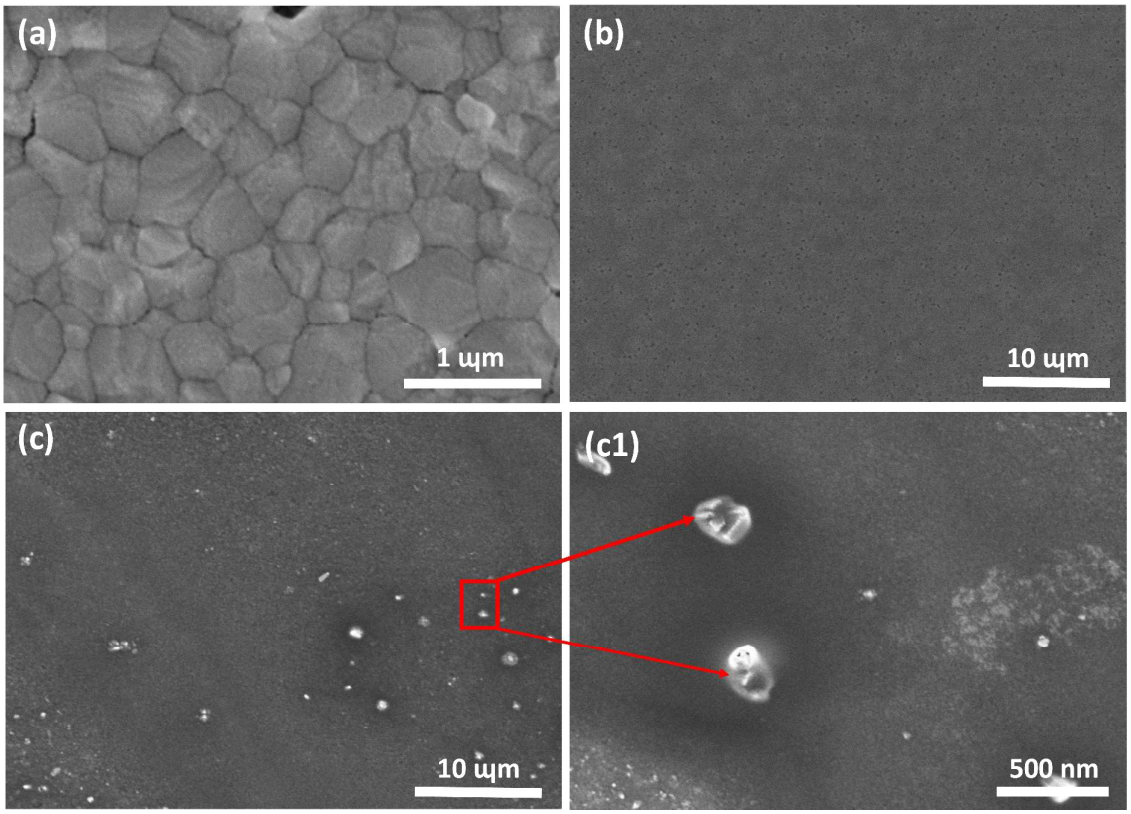

Fig. 6 (a) Surface image of $CH_3NH_3PbI_3$ perovskite film deposited on top of FTO/compact-TiO_2/mesoporous-TiO_2; (b) Top view of DPA-ANT-DPA on perovskite layer; (c) top view of Spiro-OMeTAD on perovskite, and (c1) zoomed in of top view of Spiro-OMeTAD layer, red mark highlights crystals formed due to addition of dopant. To mimics the device architecture all the layers are deposited on FTO/compact-TiO_2/mesoporous-TiO_2 substrate.

These electron microscope observations along with the contact angle measurements clearly correlate with the higher perovskite solar cell stability observed for DPA-ANT-DPA HTM based solar cells as compared to Spiro-OMeTAD HTM based solar cells. The improved homogeneous coverage of the DPA-ANT-DPA films along with de-wetting, hydrophobic nature as observed from contact angle measurements resulted in devices with much higher stability, whereas the Spiro-OMeTAD HTM films with rough, in-homogeneous surface, small to large pin-holes and increased wetting and hydrophilic nature exhibited lower stability. The good coverage along with hydrophobic nature of the DPA-ANT-DPA HTM on

View Article Online
DOI: 10.1039/C7TC05238C

the perovskite layer assures protection of the perovskite thin film layer from exposure to oxygen,[44, 45] humidity,[43] and heat.[47] In summary, the homogeneous surface morphology and de-wetting characteristics offered by the novel anthanthrone (ANT) core with extended Diphenylamine (DPA) in DPA-ANT-DPA films have contributed significantly to protecting the underneath perovskite layer from degradation.

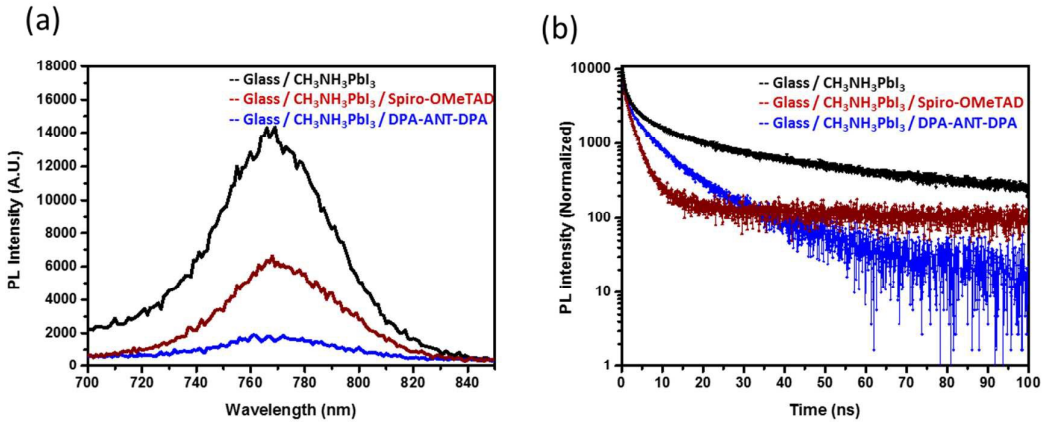

Fig. 7 (a) Steady state Photoluminescence (PL) measured on bare perovskite film (black), and hole transport layer deposited on the perovskite. Brown curve represent Spiro-OMeTAD, blue curve represents DPA-ANT-DPA, respectively, deposited on perovskite. (b) Time resolved PL taken at excitation wavelength of 765 nm of the perovskite films with different hole transport layers. A 5 mW picosecond pulsed diode laser at 635 nm was used to irradiate the perovskite and hole transport layer side.

Steady state and time resolved photoluminescence based on a simple architecture: Glass/$CH_3NH_3PbI_3$/HTM is shown in Fig. 7. In order to eliminate any quenching effect related to electron transfer to the oxide layer, we avoided to use of a TiO_2 layer while doing PL measurements. During these PL measurements, we have to make sure that the photoluminescence quenching is only caused by the hole transport layer and is not due to any other materials. All the HTL thin films were excited at 635 nm wavelength. From the data, it is quite clear that the bare perovskite film without any HTM (black curve) exhibits a high PL emission intensity as a result of the formation of good quality (crystallinity and homogeneous surface) perovskite film, which is also seen from the surface morphology of the perovskite film (Fig. 6a). On deposition of HTM on the perovskite layer, a significant reduction in PL emission was observed. Perovskite films covered with DPA-ANT-DPA HTL (blue curve)

View Article Online
DOI: 10.1039/C7TC05238C

display a stronger PL quenching (~90%) than the films covered with Spiro-OMeTAD (~60%) HTL. This effective quenching indicates a higher PL quenching ability of our newly developed DPA-ANT-TPA compared to Spiro-OMeTAD. The DPA-ANT-DPA HTM exhibits efficient exciton dissociation efficiency, comparable to that of doped Spiro-OMeTAD. This ensures a efficient charge generation and high hole mobility as well as low recombination at the DPA-ANT-DPA/$CH_3NH_3PbI_3$ interface.

The time resolved photoluminescence was performed to verify the improved hole transport properties; the results are shown in Fig. 7b. Bare perovskite films deposited on glass substrate as well as with different hole transport layers show biphasic kinetics. The fast component decays in picoseconds (due to 80 ps laser pulse) and the slower component has a time constant of 10-15 ns. The fast component represents trap filling. As the hole transfer films are deposited on bare glass - perovskite layer for direct probing, this gives us a good estimation of quenching of the photoluminescence due to hole transport layers only.

For bare perovskite sample (glass/perovskite) we have obtained high PL intensity and lifetime of 8 ns. As shown previously[48] highly crystalline, good quality perovskite sample shows a life time of ~ 8-10 ns, this confirms the quality of the perovskite films we used in this study. After the introduction of DPA-ANT-DPA hole transporting layer above the perovskite layer the average decay time (τ) shortened to ~20.2 ns. The fast decay lifetime (τ_1) of both hole transporting materials decreased from 33 ns (bare perovskite without HTL) to 18 ns for DPA-ANT-DPA and 16 ns for Spiro-OMeTAD hole transporting layer. At the same time the weight fraction increased from 3% (bare perovskite film) to 23.5% for DPA-ANT-DPA and 25.7% for Spiro-OMeTAD hole transport layers. This clearly shows the complete hole extraction as well charge dissociation exerted by our novel undoped DPA-ANT-DPA HTM is competent the traditional doped Spiro-OMeTAD.

Currently, among reported competitive D-A-D type HTMs in the literature using both planar and mesoporous devices, JY5 and JY6 HTMs in planar devices[16, 17] and BTPA-3 and H1 HTMs based mesoporous layouts exhibit lower performance.[6, 15] A brief comparison based on the similar device structure and approximately equivalent working area among our new HTM, DPA-ANT-DPA, with BTPA-3 and H1 is made and shown in Table 3. Overall, the photovoltaic performance of DPA-ANT-DPA based devices achieves the highest PCE of 11.5% among all these materials without any additives, whereas the BTPA-3-based device exhibits a close PCE of 9.81% with Li-TFSI and *t*BP as dopants. Notably, though the novel DPA-ANT-DPA and H1 have the similar HOMO energy levels, the PCE of H1 based devices

View Article Online
DOI: 10.1039/C7TC05238C

433 is very low (~5.8%) due to its small J_{sc} and the use of different type of perovskite as active
434 layers. Moreover, the device with new DPA-ANT-DPA HTM has a superior stability in
435 comparison with the reference device based on Spiro-OMeTAD.

436 **Table 3.** The comparison among promising D-A-D HTMs.

HTM[a)]	HOMO (eV)	Perovskite materials	Active area (cm^2)	Additives[b)]	V_{oc} (V)	J_{sc} (mA cm^{-2})	FF (%)	PCE (%)	Stability test[d)]	References
DPA-ANT-DPA	-5.46	$CH_3NH_3PbI_3$	0.1	None	1.00	16.2	71	11.5 (16.0)[c)]	66% (14%)[e)]	This study
BTPA-3	-5.42	$Cs_{0.05}(MA_{0.17}FA_{0.83})_{0.95}Pb(I_{0.83}Br_{0.17})_3$	0.16	Li-TFSI *t*BP	1.09	19.9	53.4	9.81 (13.2)	84% (98%)	6
		$CH_3NH_3PbBr_3$			1.44	6.66	61.5	5.91 (5.61)	75% (91%)	
H1	-5.46	$CH_3NH_3PbBr_3$	0.16	Li-TFSI *t*BP FK209	1.43	5.50	72	5.80 (6.12)	-	15

437 [a)]A typical mesoporous architecture, including FTO/compact TiO_2/mesoporous TiO_2/Perovskite/HTM/cathode,
438 was used in these studies. While Ag was the cathode in this study, Au were employed in other citations (H1,
439 BTPA-3).

440 [b)]bis(trifluoromethylsulfonyl)imide lithium salt (Li-TFSI), 4-tert-Butylpyridine (*t*BP), tris(2-(1*H*-pyrazol-1-yl)-
441 4-*tert*-butylpyridine)cobalt(III) tri[hexafluorophosphate] (FK209)

442 [c)]PCE of standard Spiro-OMeTAD

443 [d)]The percentage of the retaining performance after the ageing test (unsealed devices)

444 [e)]The percentage of the retaining performance of standard Spiro-OMeTAD

445

446 **Conclusions**

447 In summary, we have successfully designed and synthesized a new highly scalable
448 small molecular DPA-ANT-DPA HTM based on an innovative low cost anthanthrone
449 dye as a core using D-A-D molecular design. The synthesis of DPA-ANT-DPA was

View Article Online
DOI: 10.1039/C7TC05238C

elegantly conducted in a single step via a simple coupling protocol using a common anthanthrone dye as a central core and diphenylamine as end-capping units. A detailed comparison on optoelectronic properties of DPA-ANT-DPA and traditional Spiro-OMeTAD based PSCs has been performed and it has found that a HOMO energy level of DPA-ANT-DPA is close to the active perovskite energy level, guaranteeing a better hole transport ability with minimal energy offset. Upon evaluating DPA-ANT-DPA as hole transporting material, without doping in perovskite solar cell devices, the highest power conversion efficiency of 11.5% has been achieved. The DPA-ANT-DPA HTM not only exhibits a respectable performance in comparison to other undoped hole transport materials, but shows also an increased reproducibility of PSCs as compared to Spiro-OMeTAD based PSCs and a lower cost and straightforward one-step synthesis with easy purification. One of the most important features of DPA-ANT-DPA based PSC devices is their environmental stability, much higher than that of classical Spiro-OMeTAD. The reason behind the significantly higher stability of our new DPA-ANT-DPA based devices has been also investigated in detail and it was found that the hydrophobic nature and homogeneous coverage are responsible factors and they are a result of chemical structure of the central ANT core and more extended structure of DPA on the perovskite capping layer. The DPA-ANT-DPA HTM without additives resulted in V_{oc} of 1.0 V. The improved charge collection efficiency in devices prepared with DPA-ANT-DPA HTL (as seen from effective PL quenching) compared to that of the Spiro-OMeTAD HTL leads to higher short circuit current and photovoltage. By using such low cost fused anthanthrone dye, it is be possible to design new efficient, stable and low cost scalable HTMs for roll-to-roll printed perovskite solar cell modules and prototypes for large area application.

Experimental

Detailed experimental methods can be found in the Supporting Information.

Conflicts of interest

There are no conflicts to declare.

Acknowledgements

View Article Online
DOI: 10.1039/C7TC05238C

H.D.P is thankful to QUT for offering here QUTPRA scholarship to conduct his research work. Some of the data reported in this paper were obtained at the Central Analytical Research Facility operated by the Institute for Future Environments (QUT). Access to CARF is supported by generous funding from the Science and Engineering Faculty (QUT). Author S. M. J. is thankful to Welsh assembly Government funded Sêr Cymru Solar project, EPSRC grants EP/M025020/1 (Supergen Solar Challenge) and Marie-Curie COFUND fellowship for financial support. S.M. is supported by the Ministry of Education of Singapore. Additionally, this project has received funding from the European Union's Horizon 2020 research and innovation programme under the Marie Skłodowska-Curie grant agreement No 663830. P.S. is thankful to QUT for financial support and to the Australian Research Council for the Future Fellowship grant FT130101337. N.M. acknowledges the support of the Queensland government via the Q-CAS funding scheme.

View Article Online
DOI: 10.1039/C7TC05238C

References

1. Best research-cell efficiencies, http://www.nrel.gov/pv/assests/images/efficiency-chart.png (accessed: Novemeber 2017).
2. W. S. Yang, B.-W. Park, E. H. Jung, N. J. Jeon, Y. C. Kim, D. U. Lee, S. S. Shin, J. Seo, E. K. Kim, J. H. Noh and S. I. Seok, *Science*, 2017, **356**, 1376-1379.
3. N. H. Tiep, Z. Ku and H. J. Fan, *Adv. Energy Mater.*, 2016, **6**, 1501420.
4. Y.-K. Wang, Z.-C. Yuan, G.-Z. Shi, Y.-X. Li, Q. Li, F. Hui, B.-Q. Sun, Z.-Q. Jiang and L.-S. Liao, *Adv. Funct. Mater.*, 2016, **26**, 1375-1381.
5. K. Liu, Y. Yao, J. Wang, L. Zhu, M. Sun, B. Ren, L. Xie, Y. Luo, Q. Meng and X. Zhan, *Mater. Chem. Front.*, 2017, **1**, 100-110.
6. G. Wu, Y. Zhang, R. Kaneko, Y. Kojima, Q. Shen, A. Islam, K. Sugawa and J. Otsuki, *J. Phys. Chem. C*, 2017, **121**, 17617-17624.
7. H. D. Pham, H. Hu, K. Feron, S. Manzhos, H. Wang, Y. M. Lam and P. Sonar, *Solar RRL*, 2017, **1**.
8. J. Wang, K. Liu, L. Ma and X. Zhan, *Chem. Rev.*, 2016, **116**, 14675-14725.
9. S. S. Reddy, K. Gunasekar, J. H. Heo, S. H. Im, C. S. Kim, D. H. Kim, J. H. Moon, J. Y. Lee, M. Song and S. H. Jin, *Adv. Mater.*, 2016, **28**, 686-693.
10. H. D. Pham, Z. Wu, L. K. Ono, S. Manzhos, K. Feron, N. Motta, Y. Qi and P. Sonar, *Adv. Electronic Mater.*, 2017, **3**.
11. M. Saliba, S. Orlandi, T. Matsui, S. Aghazada, M. Cavazzini, J.-P. Correa-Baena, P. Gao, R. Scopelliti, E. Mosconi, K.-H. Dahmen, F. De Angelis, A. Abate, A. Hagfeldt, G. Pozzi, M. Graetzel and M. K. Nazeeruddin, *Nat. Energy*, 2016, **1**, 15017-15024.
12. S. S. Reddy, S. Shin, U. K. Aryal, R. Nishikubo, A. Saeki, M. Song and S.-H. Jin, *Nano Energy*, 2017, **41**, 10-17.
13. M. Cheng, K. Aitola, C. Chen, F. Zhang, P. Liu, K. Sveinbjörnsson, Y. Hua, L. Kloo, G. Boschloo and L. Sun, *Nano Energy*, 2016, **30**, 387-397.
14. K. Rakstys, S. Paek, P. Gao, P. Gratia, T. Marszalek, G. Grancini, K. T. Cho, K. Genevicius, V. Jankauskas, W. Pisula and M. K. Nazeeruddin, *J. Mater. Chem. A*, 2017, **5**, 7811-7815.
15. S. Carli, J. P. Baena, G. Marianetti, N. Marchetti, M. Lessi, A. Abate, S. Caramori, M. Gratzel, F. Bellina, C. A. Bignozzi and A. Hagfeldt, *ChemSusChem.*, 2016, **9**, 657-661.
16. F. Wu, Y. Ji, R. Wang, Y. Shan and L. Zhu, *Dyes Pigm.*, 2017, **143**, 356-360.
17. F. Wu, Y. Ji, C. Zhong, Y. Liu, L. Tan and L. Zhu, *Chem. Commun.*, 2017, **53**, 8719-8722.
18. J. M. Jiang, P. A. Yang, H. C. Chen and K. H. Wei, *Chem. Commun.*, 2011, **47**, 8877-8879.
19. P. Ganesan, K. Fu, P. Gao, I. Raabe, K. Schenk, R. Scopelliti, J. Luo, L. H. Wong, M. Grätzel and M. K. Nazeeruddin, *Energy Environ. Sci.*, 2015, **8**, 1986-1991.
20. S. Park, J. H. Heo, C. H. Cheon, H. Kim, S. H. Im and H. J. Son, *J. Mater. Chem. A*, 2015, **3**, 24215-24220.

View Article Online
DOI: 10.1039/C7TC05238C

21. K. Do, H. Choi, K. Lim, H. Jo, J. W. Cho, M. K. Nazeeruddin and J. Ko, *Chem. Commun.*, 2014, **50**, 10971-10974.

22. Z. Tu, X. Huang and Y. Yi, *J. Mater. Chem. C*, 2015, **3**, 1913-1921.

23. J. B. Giguere, J. Boismenu-Lavoie and J. F. Morin, *J. Org. Chem.*, 2014, **79**, 2404-2418.

24. A. Lafleur-Lambert, J.-B. Giguère and J.-F. Morin, *Macromolecules*, 2015, **48**, 8376-8381.

25. U. Koldemir, J. S. Tinkham, R. Johnson, B. Lim, H. A. Yemam, K. J. Gagnon, S. Parkin and A. Sellinger, *J. Mater. Chem. C*, 2017, **5**, 8723-8733.

26. J. B. Giguere, Q. Verolet and J. F. Morin, *Chem. Eur. J.*, 2013, **19**, 372-381.

27. A. D. Becke, *J. Chem. Phys.*, 1993, **98**, 5648-5652.

28. P. Hohenberg and W. Kohn, *Phys. Rev.* , 1964, **136**, B864-B871.

29. W. Kohn and L. Sham, *Phys. Rev.* , 1965, **140**, A1133-A1138.

30. S. Paek, M. A. Rub, H. Choi, S. A. Kosa, K. A. Alamry, J. W. Cho, P. Gao, J. Ko, A. M. Asiri and M. K. Nazeeruddin, *Nanoscale*, 2016, **8**, 6335-6340.

31. F. M. Jradi, X. Kang, D. O'Neil, G. Pajares, Y. A. Getmanenko, P. Szymanski, T. C. Parker, M. A. El-Sayed and S. R. Marder, *Chem. Mater.*, 2015, **27**, 2480-2487.

32. P. Qin, H. Kast, M. K. Nazeeruddin, S. M. Zakeeruddin, A. Mishra, P. Bäuerle and M. Grätzel, *Energy Environ. Sci.*, 2014, **7**, 2981–2985.

33. C. Steck, M. Franckevičius, S. M. Zakeeruddin, A. Mishra, P. Bäuerlea and M. Grätzel, *J. Mater. Chem. A*, 2015, **3**, 17738-17746.

34. K. Rakstys, M. Saliba, P. Gao, P. Gratia, E. Kamarauskas, S. Paek, V. Jankauskas and M. K. Nazeeruddin, *Angew. Chem. Int. Ed. Engl.*, 2016, **55**, 1-6.

35. D. Shi, X. Qin, Y. Li, Y. He, C. Zhong, J. Pan, H. Dong, W. Xu, T. Li, W. Hu, J.-L. Brédas and O. M. Bakr, *Sci. Adv.*, 2016, **2**, e1501491.

36. S. Paek, P. Qin, Y. Lee, K. T. Cho, P. Gao, G. Grancini, E. Oveisi, P. Gratia, K. Rakstys, S. A. Al-Muhtaseb, C. Ludwig, J. Ko and M. K. Nazeeruddin, *Adv. Mater.*, 2017, **29**, 1606555.

37. N. J. Jeon, J. H. Noh, Y. C. Kim, W. S. Yang, S. Ryu and S. I. Seok, *Nat. Mater.*, 2014, **13**, 897-903.

38. W.-J. Yin, J.-H. Yang, J. Kang, Y. Yan and S.-H. Wei, *J. Mater. Chem. A*, 2015, **3**, 8926-8942.

39. J. Liu, Y. Wu, C. Qin, X. Yang, T. Yasuda, A. Islam, K. Zhang, W. Peng, W. Chen and L. Han, *Energy Environ. Sci.*, 2014, **7**, 2963–2967.

40. S. Kazim, F. J. Ramos, P. Gao, M. K. Nazeeruddin, M. Grätzel and S. Ahmad, *Energy Environ. Sci.*, 2015, **8**, 1816-1823.

41. M. Franckevičius, A. Mishra, F. Kreuzer, J. Luo, S. M. Zakeeruddin and M. Grätzel, *Mater. Horiz.*, 2015, **2**, 613-618.

42. Y. Hou, H. Zhang, W. Chen, S. Chen, C. O. R. Quiroz, H. Azimi, A. Osvet, G. J. Matt, E. Zeira, J. Seuring, N. Kausch-Busies, W. Lövenich and C. J. Brabec, *Adv. Energy Mater.*, 2015, **5**, 1500543.

View Article Online
DOI: 10.1039/C7TC05238C

43. J. S. Manser, M. I. Saidaminov, J. A. Christians, O. M. Bakr and P. V. Kamat, *Acc. Chem. Res.*, 2016, **49**, 330-338.

44. J. Yang, B. D.Siempelkamp, D. Liu and L. K. Timothy, *ACS Nano*, 2015, **9**, 1955-1963.

45. T. Leijtens, T. Giovenzana, S. N. Habisreutinger, J. S. Tinkham, N. K. Noel, B. A. Kamino, G. Sadoughi, A. Sellinger and H. J. Snaith, *ACS Appl. Mater. Interfaces*, 2016, **8**, 5981-5989.

46. B. Xu, J. Zhang, Y. Hua, P. Liu, L. Wang, C. Ruan, Y. Li, G. Boschloo, E. M. J. Johansson, L. Kloo, A. Hagfeldt, A. K. Y. Jen and L. Sun, *Chem*, 2017, **2**, 676-687.

47. W. H. Nguyen, C. D. Bailie, E. L. Unger and M. D. McGehee, *J. Am. Chem. Soc.*, 2014, **136**, 10996-11001.

48. S. M. Jain, Z. Qiu, L. Häggman, M. Mirmohades, M. B. Johansson, T. Edvinsson and G. Boschloo, *Energy Environ. Sci.*, 2016, **9**, 3770-3782.